Current Ripple Analysis and Controller Design for Grid-Connected Converters Considering the Soft-Saturation Nature of the Powder Cores

Qikang Wei, Bangyin Liu, *Member, IEEE*, and Shanxu Duan, *Senior Member, IEEE*

***Abstract*—The powder-core-based inductor has a wide inductance variation due to the soft-saturation nature when subjected to varying load current. Under such a condition, the current ripple is influenced, and the conventional inductor design principle may be inaccurate. Besides, the voltage of the inductor is distorted. Also, the bandwidth of the controller is hard to determine. In this paper, the current ripple under the condition of wide inductance variation is analyzed, and its change rule is revealed; then, a new inductance design principle is proposed. The harmonic components for the three-phase converter with the powder core inductor are investigated, and the harmonic characteristic of the input current is analyzed. According to the current harmonic characteristic, the resonance controllers are introduced to eliminate harmonics, and the quality of the current is improved. Besides, the bandwidth of the controller is found to vary with the output power. Then, a compensation method is proposed to eliminate the influence of inductance variation on the bandwidth. The experimental results verify the analysis.**

***Index Terms*—Converter, digital control, inductor, stability.**

I. Introduction

THE three-phase pulse width modulation (PWM) converter has been widely applied to power systems due to its characteristics such as low harmonic distortion of current, bidirectional power flow control, and reactive power adjustment [1]–[7]. The inductor is a vital part of the converter, and it influences the waveform quality of the input current, efficiency, stability, and so on. The core materials of the inductor generally can be ferrite, molybdenum permalloy powder, *KoolMμ* or high flux [8]. Compared with ferrite cores, the powder cores have higher saturation flux density and a softer saturation curve. They are also less sensitive to temperature changes. And the distributed air gap makes the powder cores suitable for high-frequency applications. So the powder core inductor is widely used in a high-frequency converter. However, the inductance of the powder core inductor varies over a wide range when the value of ac current changes in a period. For example, the permeability of *KoolMμ* descends when the magnetizing force increases, as shown in Fig. 1 [9]. The performance of the converter is different when the inductance varies with current.

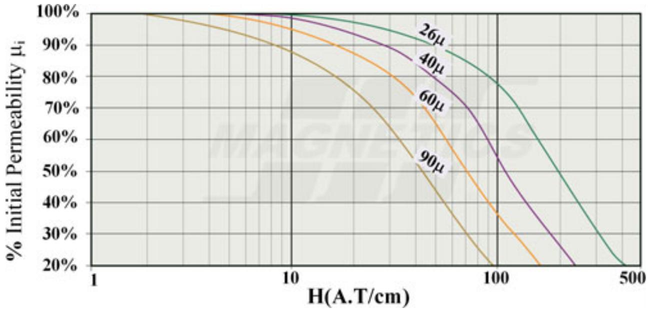

Fig. 1. Permeability versus dc bias curves (*KoolMμ* shapes).

A vital function of the inductor is to limit the maximum current ripple. If the current ripple is too large, the input current will be distorted and the inductor loss will increase. So, the current ripple is usually limited. The current ripple under different modulations has been investigated [10]–[12]. The inductor is mostly supposed to be constant in these works. Few literature studies have explored the current ripple when the three-phase inductances are different and vary with current. When the converter has a wide inductance variation, not only the current ripple is influenced, but also the input current is distorted. So, it is important to study the characteristics of the inductor [13]. Jayalath *et al.* [14] model the powder core inductors using finite-element analysis, and they highlight the importance of considering the soft-saturation nature of powder materials when designing inductors for the inverter. The describing function method is used to estimate the nonlinear inductance for large power filter design [15]. In [16], this method is used to analyze two different nonlinearities: saturation for high currents and a light nonlinearity. Then, the model based on the Volterra series expansion is developed. Many methods have been proposed to mitigate the effects of the inductance variation. The resonance

---

Manuscript received June 24, 2017; revised October 24, 2017; accepted November 16, 2017. Date of publication November 27, 2017; date of current version July 15, 2018. This work was supported in part by the National Key R&D Program of China under Grant 2016YFB0900400, in part by the National Natural Science Foundation of China under Grant 51777084, in part by the Lite-On Research Program under Grant HUST201501. Recommended for publication by Associate Editor J. A. Cobos. *(Corresponding author: Bangyin Liu.)*

The authors are with the State Key Laboratory of Advanced Electromagnetic Engineering and Technology, School of Electrical and Electronic Engineering, Huazhong University of Science and Technology, Wuhan 430074, China (e-mail: weiqkang@hust.edu.cn; lby@hust.edu.cn; duanshanxu@hust.edu.cn).

Color versions of one or more of the figures in this paper are available online at http://ieeexplore.ieee.org.

Digital Object Identifier 10.1109/TPEL.2017.2777906

controllers are applied to compensate the five, seven, and 11 harmonic orders in [17]. However, it is not explained why the current is distorted at the frequency of these harmonic orders. And to improve the quality of the input current, an online inductance estimation is offered. In [18], Wu *et al.* present a predictive current controller. The parameters should be tabulated offline to reduce the CPU operational time and keep accuracy. Then, they propose the D-Σ digital control [19]–[24]. It summarizes the inductor–current variations over one switching cycle to derive control laws directly. To ensure stable operation, the inductances corresponding to various inductor currents are measured and tabulated into a single-chip microcontroller for tuning loop gain cycle by cycle [21]. This D-Σ digital control can not only be suitable for inductance variation, but can be further applied in a transformerless inverter to suppress the circulating current [19].

The current ripple considering a wide inductance variation is investigated in this paper. The maximum current ripple is discussed, and the filter design principle is deduced for engineering application. Then, the model of the powder core inductor considering the soft-saturation nature is developed, which is based on the Fourier series expansion. With the help of the model, the characteristic of voltage harmonic for a three-phase converter is discussed, and the resonance controller is applied to improve the quality of the current waveform. Another influence of the powder core inductor is that the bandwidth of the controller is hard to determine. To solve this problem, the mean value of the inductance is estimated according to the model to determine the bandwidth. However, the mean value of the inductance varies with the output power and influences the performance of the converter. Then, a compensation method that can eliminate the influence of the inductance variation on the stability is proposed.

This paper is organized as follows. In Section II, the current ripple considering wide inductance variation is discussed, and the filter design principle is developed. In Section III, the model of the filter inductor considering the soft-saturation nature of powder core material is develop, and a control strategy is proposed to eliminate the influence of the variation of inductance. The experimental results and conclusions of the work are presented in Sections IV and V, respectively.

II. CURRENT RIPPLE ANALYSIS AND FILTER DESIGN CONSIDERING THE VARIATION OF INDUCTANCE

A. Analysis of Current Ripple

Suppose that the grid is ideal and the power factor is 1. The harmonic components of the modulation wave are neglected to simplify the analysis. The modulation waves of the three-phase converter are shown in Fig. 2. As the current is symmetrical, the maximum current ripple is the same for each phase. Thus, only the current ripple of phase A is considered. When the angle of current varies, the current ripple changes periodically. And regions I and II form one period. For the modulation wave in region I, phase C is the largest and phase B the least. But, in region II, the modulation wave of phase A is the largest and phase B the least.

The equivalent circuit of the three-phase converter is shown in Fig. 3. s_i $(i = a, b, c)$ stands for the switch function. $s_i = 1$ means that the switch is ON and $s_i = 0$ for OFF. The voltage of point N can be deduced as

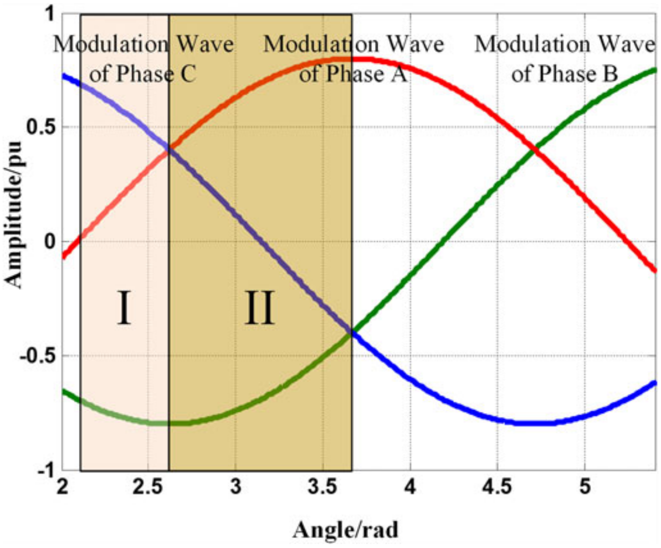

Fig. 2. Modulation wave of a three-phase converter.

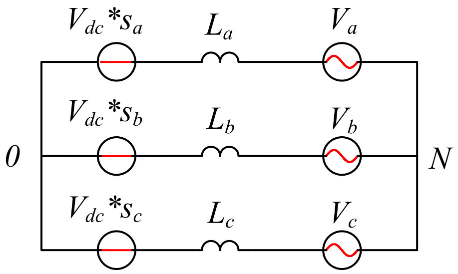

Fig. 3. Equivalent circuit of a three-phase converter.

$$V_N = \frac{L_b L_c V_{\mathrm{dc}} s_a + L_a L_c V_{\mathrm{dc}} s_b + L_a L_b V_{\mathrm{dc}} s_c}{L_b L_c + L_a L_c + L_a L_b} - \frac{L_b L_c V_a + L_a L_c V_b + L_a L_b V_c}{L_b L_c + L_a L_c + L_a L_b}. \tag{1}$$

It should be noted that the inductance of L_a, L_b, and L_c are different as the current of three phases differ. According to Kirchhoff's voltage law, it is satisfied that

$$V_{\mathrm{dc}} s_a = L_a \frac{di_a}{dt} + V_a + V_N. \tag{2}$$

The current ripple Δi_a can be solved by putting s_a, s_b, and s_c into (2). The switching function is determined by the modulation method. Thus, the current ripple changes with different modulation methods. The sinusoidal PWM (SPWM) is considered in this approach. There are five cases of the switch state identified as cases a, b, c, d, and e, as shown in Fig. 4. Putting s_a, s_b, and s_c into (2) and solving it, the variation of current in

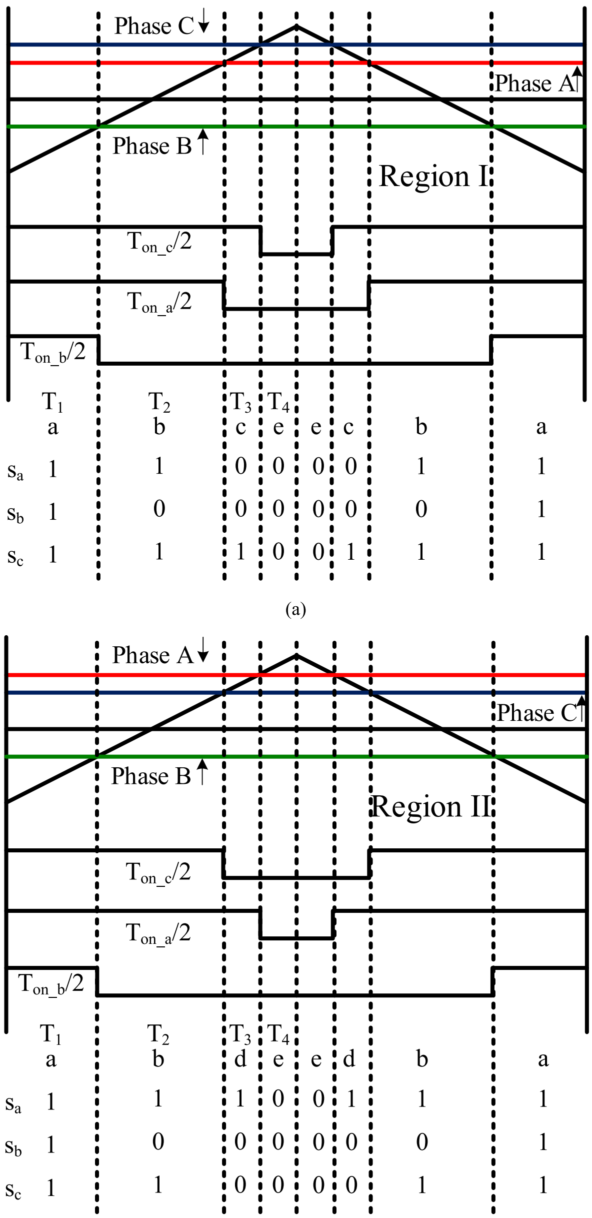

(a)

(b)

Fig. 4. Switch state for SPWM. (a) Region I. (b) Region II.

each case is

$$
\begin{cases}
\text{case} \quad a\,(s_a = 1, s_b = 1, s_c = 1): \\
|\Delta i_a| = \left|\frac{T_1}{L_a}\left(\frac{(L_bL_cV_a + L_aL_cV_b + L_aL_bV_c)}{L_bL_c + L_aL_c + L_aL_b} - V_a\right)\right| \\
\text{case} \quad b\,(s_a = 1, s_b = 0, s_c = 1): \\
|\Delta i|_a = \left|\frac{T_2}{L_a}\left(\frac{(L_bL_cV_a + L_aL_cV_b + L_aL_bV_c) + V_{\mathrm{dc}}L_aL_c}{L_bL_c + L_aL_c + L_aL_b} - V_a\right)\right| \\
\text{case} \quad c\,(s_a = 0, s_b = 0, s_c = 1): \\
|\Delta i_a| = \left|\frac{T_3}{L_a}\left(\frac{(L_bL_cV_a + L_aL_cV_b + L_aL_bV_c) - V_{\mathrm{dc}}L_aL_b}{L_bL_c + L_aL_c + L_aL_b} - V_{\mathrm{a}}\right)\right| \\
\text{case} \quad d\,(s_a = 1, s_b = 0, s_c = 0): \\
|\Delta i_a| = \\
\left|\frac{T_3}{L_a}\left(\frac{(L_bL_cV_a + L_aL_cV_b + L_aL_bV_c) + V_{\mathrm{dc}}(L_aL_c + L_aL_b)}{L_bL_c + L_aL_c + L_aL_b} - V_a\right)\right| \\
\text{case} \quad e\,(s_a = 0, s_b = 0, s_c = 0): \\
|\Delta i_a| = \left|\frac{T_4}{L_a}\left(\frac{(L_bL_cV_a + L_aL_cV_b + L_aL_bV_c)}{L_bL_c + L_aL_c + L_aL_b} - V_a\right)\right|
\end{cases}
\tag{3}
$$

TABLE I
VARIATION TENDENCY OF CURRENT IN A PERIOD

Region I								
case	a	b	c	e	e	c	b	A
Δi_a	↓	↑	↓	↓	↓	↓	↑	↓
Region II								
Case	a	b	d	e	e	d	b	a
Δi_a	↓	↑	↑	↓	↓	↑	↑	↓

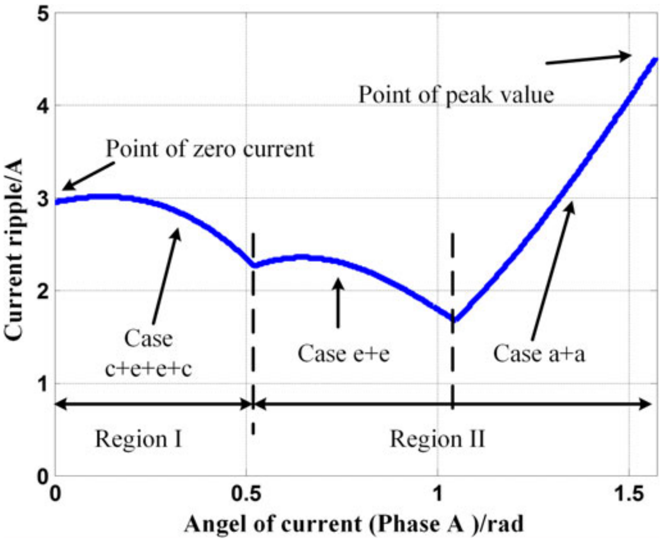

Fig. 5. Current ripple versus angle (phase A).

and the time for each case is as follows:

$$
\begin{cases}
T_1 = T_{\mathrm{on}\_b}/2 \\
T_2 = \begin{cases} (T_{\mathrm{on}\_a} - T_{\mathrm{on}\_b})/2 & \text{Region I} \\ (T_{\mathrm{on}\_c} - T_{\mathrm{on}\_b})/2 & \text{Region II} \end{cases} \\
T_3 = \begin{cases} (T_{\mathrm{on}\_c} - T_{\mathrm{on}\_a})/2 & \text{Region I} \\ (T_{\mathrm{on}\_a} - T_{\mathrm{on}\_c})/2 & \text{Region II} \end{cases} \\
T_4 = \begin{cases} (T - T_{\mathrm{on}\_c})/2 & \text{Region I} \\ (T - T_{\mathrm{on}\_a})/2 & \text{Region II.} \end{cases}
\end{cases}
\tag{4}
$$

The turn-on time for each switch is as follows:

$$
\begin{cases}
T_{\mathrm{on}\_a} = (0.5 + m_d \sin(\omega t))\,T \\
T_{\mathrm{on}\_b} = (0.5 + m_d \sin(\omega t - 120^\circ))\,T \\
T_{\mathrm{on}\_c} = (0.5 + m_d \sin(\omega t + 120^\circ))\,T
\end{cases}
\tag{5}
$$

where m_d is the modulation ratio and T stands for the period. According to (3), the variation tendency of current is further displayed in Table I. The current can increase or fall in a period. If the maximum $|\Delta i_a|$ is defined as the current ripple, the current ripple is the summation of cases c and e for region I and the maximum of cases a and e for region II, as shown in Table I. And the current ripple versus current angle can be plotted, as shown in Fig. 5. Although Fig. 5 is a special case, it reveals the variation tendency of the current ripple. In fact, the V_a and

T_1, T_4 are the dominate components for cases a and e in (3), which determine that the maximum current ripple occurs at the peak value of the current.

B. Inductance Design Principle

The maximum current ripple is the concern in the design of inductance. For the engineering design, the maximum current ripple is limited to a certain value. According to the change tendency of the current ripple, the maximum current ripple appears at the point, where the current of phase A reaches the peak value or around zero. Combine (3)–(5) and solve the current ripple as Table I defines. At the point where the current is zero, the inductance satisfies

$$2{*}L\left(i_a\right)\big|_{i_a=0} + L\left(i_a\right)\big|_{i_a=i_m\sin(60^\circ)} > \frac{\sqrt{3}}{2}\frac{V_g T}{\Delta i} \tag{6}$$

and at the point where the current reaches peak value, the inductance satisfies

$$2{*}L\left(i_a\right)\big|_{i_a=i_m} + L\left(i_a\right)\big|_{i_a=i_m\sin(30^\circ)} > \frac{3V_g T}{\Delta i}\frac{V_{\mathrm{dc}}-V_g}{2V_{\mathrm{dc}}} \tag{7}$$

where i_m is the amplitude of the current and V_g is the amplitude of the grid voltage. From (6) and (7), if $V_g = 0.42V_{\mathrm{dc}}$, the right parts are equal. But considering the characteristic of powder cores, when the current is zero, the inductance may be several times bigger than that when the current reaches peak value. So, for general design, if (7) is satisfied, (6) can also be satisfied, and thus, (7) can be used to guide the inductance design. For the experimental setup, suppose that the maximum current ripple is 20% of the rated current; then, the inductance calculated from (7) is

$$2{*}0.4\,\mathrm{mH} + 0.72\,\mathrm{mH} > \frac{3V_g T}{\Delta i}\frac{V_{\mathrm{dc}}-V_g}{2V_{\mathrm{dc}}} = 1.49\,\mathrm{mH}. \tag{8}$$

The minimum inductance $L\left(i_a = i_m\right)$ is 0.4 mH. The inductance $L\left(i_a = i_m \sin 30^\circ\right)$ is 0.72 mH, which is estimated according to the curve in Fig. 1. For the conventional inductance design, the inductances of the three phases are supposed to be identical. When the inductance of phase A reaches the minimum value $L\left(i_a = i_m\right)$, the inductances of phases B and C are also supposed to be $L\left(i_a = i_m\right)$, while in this approach, the inductances of phases B and C are considered to be $L\left(i_a = i_m \sin 30^\circ\right)$. As the actual inductances ($L\left(i_a = i_m \sin 30^\circ\right)$) are larger than the supposed ones ($L\left(i_a = i_m\right)$), the actual current ripple is smaller than the calculated result from the conventional design principle. According to the conventional design principle, the minimum inductance should be 0.5 mH to satisfy the current ripple requirement ($3 \times L\left(i_a = i_m\right) > 1.49\,\mathrm{mH}$). Obviously, the result of (7) is smaller. The value of inductance decreases by 20%. So, a smaller value of inductance can be obtained with the proposed design principle.

III. CONTROL METHOD FOR GRID-CONNECTED CONVERTERS WITH THE POWDER CORE FILTER INDUCTOR

A. Modeling of the Powder Core Inductor With the Soft-Saturation Nature

If the inductor is powder core, the inductance varies periodically with ac current. Suppose that the current of phase A is $i_a = i_m \sin\omega t$; the inductance of phase A is an even symmetry function. According to the Fourier series, the inductance can be expanded as

$$L\left(\omega t\right) = L_0 + \sum_{n=1}^{\infty} L_n \cos\left(n\omega t\right). \tag{9}$$

To solve (9), the value of inductance ($L\left(\omega t\right)$) is needed. In this approach, the inductance is linearized according to the permeability versus dc bias curves shown in Fig. 1. The error is acceptable, and it is verified with experiment in Section V. According to the powder core manual, the fit formula of permeability versus dc bias curve is

$$u = a + bH + cH^2 + dH^3 + eH^4. \tag{10}$$

a, b, c, d, and e are the coefficients (for the experimental setup, $a = 1, b = -4.445\mathrm{e}-3, c = -8.762\mathrm{e}-5, d = 9.446\mathrm{e}-7$, and $d = 2.616\mathrm{e}-9$.). The fundamental component is the main part of current. Thus, the effect of the harmonic components of the current on the inductance can be neglected. So, the inductance can be described as

$$\begin{aligned} L\left(\omega t\right) &= L_{\max}(a + bm_e\left|I_m\sin\omega t\right| + c{m_e}^2\left|I_m\sin\omega t\right|^2 \\ &\quad + d{m_e}^3\left|I_m\sin\omega t\right|^3 + \mathrm{e}{m_e}^4\left|I_m\sin\omega t\right|^4) \end{aligned} \tag{11}$$

where $L_{\max}$ is the inductance when current is zero. m_e is a constant value, which is the ratio of number of turns to magnetic path length (N/l_e). Combining (9) and (11), the result is

$$L\left(\omega t\right) = L_0 + \sum_{n=1}^{\infty} L_{2n}\cos 2n\omega t \tag{12}$$

where the coefficients are

$$\begin{aligned} &L_0 = \\ &L_{\max}\left(a + \frac{2}{\pi}bm_eI_m + \frac{1}{2}c{m_e}^2{I_m}^2 + \frac{4}{3\pi}d{m_e}^3{I_m}^3 + \frac{3}{8}e{m_e}^4{I_m}^4\right) \\ &L_2 = \\ &L_{\max}\left(-\frac{4}{3\pi}bm_eI_m - \frac{1}{2}c{m_e}^2{I_m}^2 - \frac{8}{5\pi}d{m_e}^3{I_m}^3 - \frac{1}{2}e{m_e}^4{I_m}^4\right) \\ &L_4 = L_{\max}\left(-\frac{4}{15\pi}bm_eI_m + \frac{8}{35\pi}d{m_e}^3{I_m}^3 + \frac{1}{8}e{m_e}^4{I_m}^4\right) \\ &L_{2n} = L_{\max}\begin{pmatrix} -\frac{4}{(2n-1)(2n+1)\pi}bm_eI_m \\ +\frac{24d{m_e}^3{I_m}^3}{(2n-3)(2n-1)(2n+1)(2n+3)\pi} \end{pmatrix} n > 2. \end{aligned} \tag{13}$$

Equation (12) is the model in this approach. In the following description, the mean value L_0 is called the effective inductance and the others the fluctuating inductances.

TABLE II
HARMONIC COMPONENTS OF THE VOLTAGE

	Phase A	Phase B	Phase C	order	Phase sequence
n = $3k$	$\cos((6k+1)\omega t)$	$\cos((6k+1)\omega t + (-6k-1)\times 2\pi/3)$	$\cos((6k+1)\omega t + (6k+1)\times 2\pi/3)$	$6k+1$	Positive sequence
	$\cos((6k-1)\omega t)$	$\cos((6k-1)\omega t + (-6k+1)\times 2\pi/3)$	$\cos((6k-1)\omega t + (6k-1)\times 2\pi/3)$	$6k-1$	Negative sequence
n = $3k+1$	$\cos((6k+3)\omega t)$	$\cos((6k+3)\omega t + (-6k-3)\times 2\pi/3)$	$\cos((6k+3)\omega t + (6k+3)\times 2\pi/3)$	$6k+3$	Zero sequence
	$\cos((6k+1)\omega t)$	$\cos((6k+1)\omega t + (-6k-1)\times 2\pi/3)$	$\cos((6k+1)\omega t + (6k+1)\times 2\pi/3)$	$6k+1$	Positive sequence
n = $3k-1$	$\cos((6k-1)\omega t)$	$\cos((6k-1)\omega t + (-6k+1)\times 2\pi/3)$	$\cos((6k-1)\omega t + (6k-1)\times 2\pi/3)$	$6k-1$	Negative sequence
	$\cos((6k-3)\omega t)$	$\cos((6k-3)\omega t + (-6k+3)\times 2\pi/3)$	$\cos((6k-3)\omega t + (6k-3)\times 2\pi/3)$	$6k-3$	Zero sequence

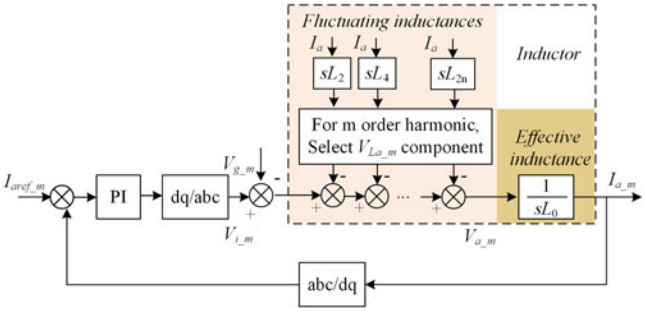

Fig. 6. Equivalent function block of the wide variation inductor.

Suppose that the current of phase A is described as $I_m \sin(m\omega t)$. Then, according to (12), the voltages of the inductor are shown in (14) shown at the bottom of this page.

V_{La}, V_{Lb}, and V_{Lc} are the voltages of the three-phase inductors. From (14), the voltage caused by the effective inductance (L_0) has the same frequency ($m\omega$) as the current. Its function is just like the conventional inductor. However, the voltage caused by the fluctuating inductances (L_{2n}) has a different frequency ($(2n \pm m)\omega$) compared to the current. Considering the fundamental current ($m = 1$), the harmonic components of the voltage are listed in Table II. According to Table II, the voltage of the fluctuating inductances contains 3, 5, …, $2n-1$ order harmonic components. If the harmonic order is $6k - 1$, the voltage harmonic is a negative sequence, and if the harmonic order is $6k + 1$, the voltage harmonic is a positive sequence. The fundamental current is large and will result in considerable harmonic voltage. The harmonic voltage will further generate harmonic current according to (14). So, the fluctuating inductances bring harmonic voltage disturbances into the converter and worsen the quality of the output current.

For a closed-loop control block shown in Fig. 6, the signal flowing through the closed loop keeps the frequency invariant. Supposing that the output signal of the converter is an m-order harmonic voltage (V_{i_m}), for a certain current (I_a contains all the harmonic currents), the voltages of the fluctuating inductances contain all the harmonic voltage. But for this closed loop, only the m-order components (V_{La_m}) will work as disturbances. So, the output signal (I_{a_m}) is decided by the effective inductance L_0. The fluctuating inductances (L_{2n}) are looked upon disturbances for the controller design.

B. Compensation Controller Eliminating the Influence of the Wide Inductance Variation

The fluctuating inductances (L_{2n}) cause harmonic currents and worsen the quality of output waveform. As analyzed above, the voltage of the inductor contains ($6k$ – 1)-order negative-sequence harmonics and $6k + 1$ positive-sequence harmonics. They become $6k$-order harmonics in the synchronous frame. The resonance controllers are able to tune at $6k$-order harmonic frequencies to regulate the current with high waveform quality [26], [27]. A proportional–integral–resonant controller is applied to inhibit the negative-sequence components in ac output currents of parallel modules [28]. Safamehr *et al.* [17] have applied a proportional–resonance (PR) controller to improve the quality of the current with a nonlinear inductor. As the fifth-, seventh-, 11th-, and 13th-order harmonics are the main components, the sixth-order and 12-order resonance controllers in the synchronous frame are applied to tune the current waveform. The control block is shown in Fig. 7.

The inductance varies with current, making it hard to determine the bandwidth of the controller. As analyzed above, the mean value of the inductance called effective inductance can determine the bandwidth. For an ac current with a fixed amplitude value, the effective inductance is also fixed. Thus, the bandwidth of the controller with the fixed output power can be determined. However, when the output power (or the amplitude

$$\begin{cases} V_{La} = L_a \frac{di_a}{dt} = m\omega L_0 I_m \cos(m\omega t) + \frac{m\omega I_m}{2} \sum\limits_{n=1}^{\infty} L_{2n} \left(\cos(2n+m)\omega t + \cos(2n-m)\omega t\right) \\ V_{Lb} = L_b \frac{di_b}{dt} \\ \quad = m\omega L_0 I_m \cos\left(m\omega t - \frac{2\pi}{3}\right) + \frac{m\omega I_m}{2} \sum\limits_{n=1}^{\infty} L_{2n} \left(\cos\left((2n+m)\omega t + (-2n-1)\frac{2\pi}{3}\right) + \cos\left((2n-m)\omega t + (-2n+1)\frac{2\pi}{3}\right)\right) \\ V_{Lc} = L_c \frac{di_c}{dt} \\ \quad = m\omega L_0 I_m \cos\left(m\omega t + \frac{2\pi}{3}\right) + \frac{m\omega I_m}{2} \sum\limits_{n=1}^{\infty} L_{2n} \left(\cos\left((2n+m)\omega t + (2n+1)\frac{2\pi}{3}\right) + \cos\left((2n-m)\omega t + (2n-1)\frac{2\pi}{3}\right)\right) \end{cases} \tag{14}$$

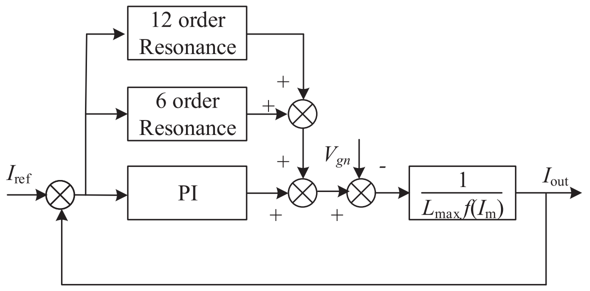

Fig. 7. Control block of the original converter in the synchronous frame.

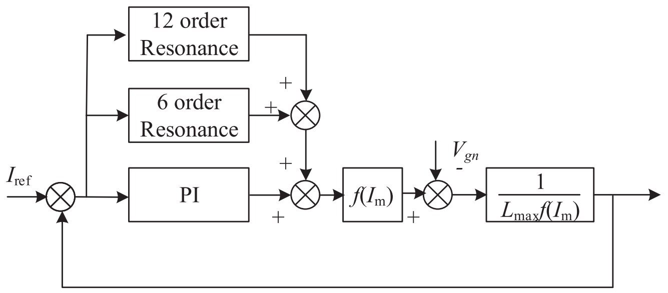

Fig. 9. Control block of the converter with compensation.

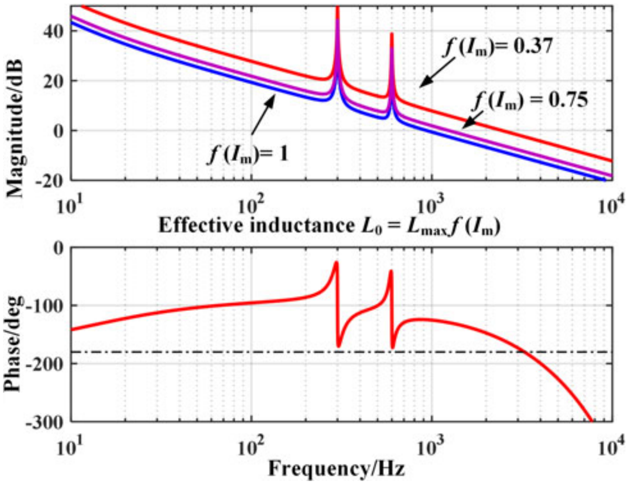

Fig. 8. Bode plot of the converter in the condition of inductance variation.

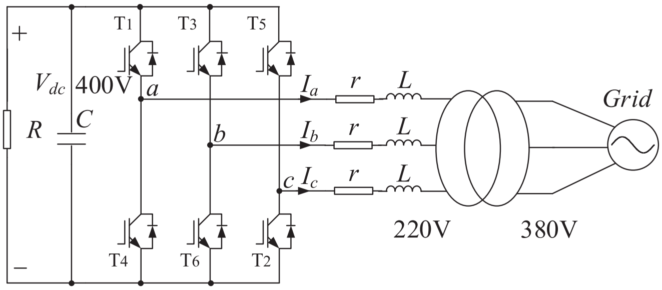

Fig. 10. System diagram of a three-phase converter.

TABLE III
KEY PARAMETERS OF THE SYSTEM

Symbol	Parameter	Value
L	Inductor	0.4–1.06 mH
f_s	Switching frequency	20 kHz
f_o	Fundament frequency	50 Hz
V_{dc}	DC-bus voltage	400 V
f_{ctrl}	Controlling frequency	20 kHz
T_{delay}	Delay time	1.5T
V_g	RMS of the grid phase voltage	127 V
P	Rated power	6.6 kW
n	Turn ratio	380:220
r	Equivalent resistance	0.2 Ω
R	Load resistance	24 Ω

of the current) changes, the mean value of the inductance will also change. Thus, the bandwidth of the controller is not fixed, and it changes with the output power. According to (13), the effective inductance varies with output power. The relation can be rewritten as

$$\begin{cases} L_0 = L_{\max} f(I_m) \\ f(I_m) \\ = a + \frac{2}{\pi} b m_e I_m + \frac{1}{2} c {m_e}^2 {I_m}^2 + \frac{4}{3\pi} d {m_e}^3 {I_m}^3 + \frac{3}{8} e {m_e}^4 {I_m}^4. \end{cases} \tag{15}$$

$f(I_m)$ stands for the variation function of the effective inductance. a, b, c, d, e, and m_e are constants. According to (15), $f(I_m)$ changes with the amplitude of the current (I_m). Special attention is required to ensure that the converter is working well from no load to full load. For example, the effective inductance is 1.06 mH when the converter works without load, and it becomes 0.5 mH when the converter runs with full load. The bode plot of the converter considering inductance variation is shown in Fig. 8. It is calculated from the transfer function according to the control block in Fig. 6. The larger the output power, the smaller the effective inductance ($L_0 = L_{\max} f(I_m)$). When the effective inductance is large, the crossover frequency is small and might be too close to the resonance frequency. The PR controller may excite low-frequency instability when the bandwidth is lower than the resonance frequency [25]. On the other side, the converter cannot work well when the effective inductance is small. On the other side, the converter cannot work well when the effective inductance is small, because the smaller effective inductance will result in a larger crossover frequency and a smaller phase margin. So, the PI parameters must be carefully chosen to ensure that the converter is working well no matter how much the load is. However, there might be no satisfied PI parameters especially when the variation range of the effective inductance is large. Thus, a controller that can compensate the variation of the effective inductance is required.

As Fig. 9 shows, the component $f(I_m)$ is added to the control loop. The value of $f(I_m)$ can be acquired by putting the current reference signal into (15) ($I_{ref} = I_m$). With $f(I_m)$, the crossover frequency theoretically remains invariant no matter how the effective inductance changes. Thus, the converter performance can be accurately designed.

IV. EXPERIMENTAL VERIFICATION

For the experimental verification, a three-phase converter controlled by TMS320F28335 DSP shown in Fig. 10 is performed. The key parameters of the system are listed in Table III, and the experimental setup is shown in Fig. 11.

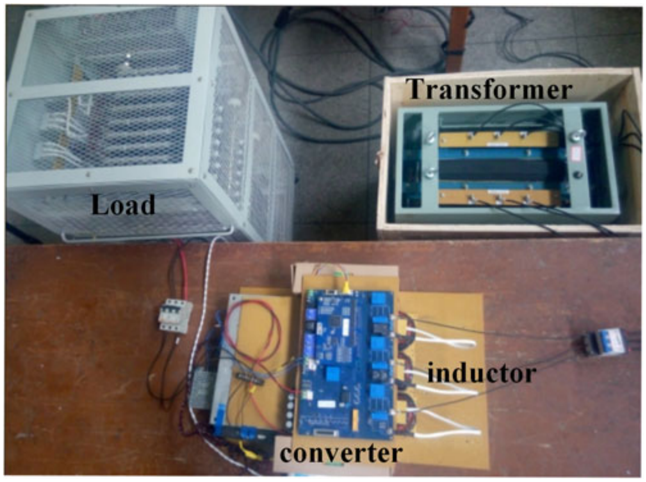

Fig. 11. Experimental setup of a three-phase converter.

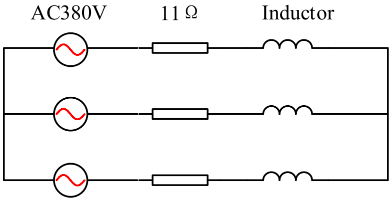

Fig. 12. Experiment circuit to test the inductor voltage with almost sine current.

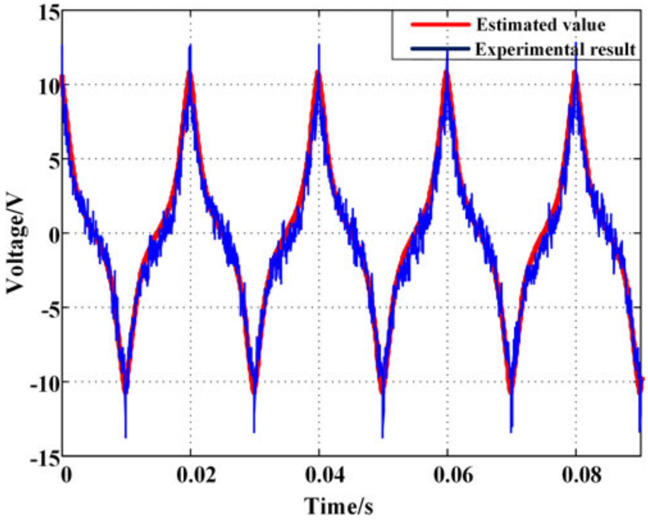

Fig. 13. Experimental result and estimated value of the inductor voltage.

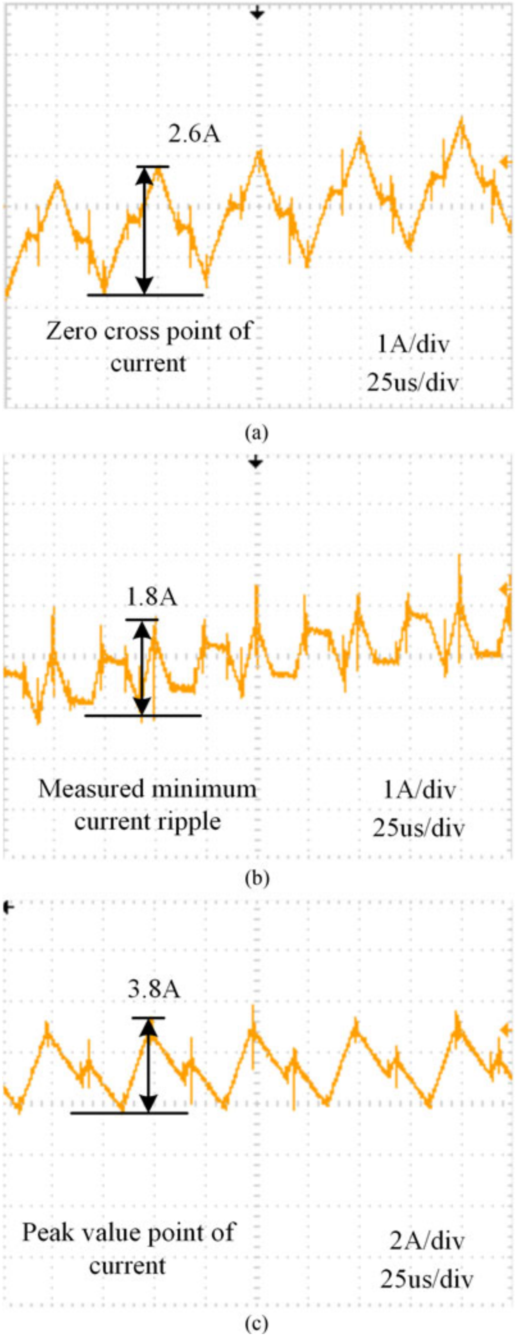

Fig. 14. Experimental result of current ripple (SPWM). (a) Zero cross point of current. (b) Measured minimum current ripple. (c) Peak value point of current.

The first experiment is performed to verify the accuracy of using (11), i.e., the permeability versus dc bias curves shown in Fig. 1, to estimate inductance. As analyzed above, the inductance varies with current. For a sine current, the voltage of the inductor is no longer a sine waveform, and the voltage can be estimated with the help of (11). The experiment circuit is shown in Fig. 12. The value of the resister is much larger than inductive reactance. Thus, the waveform of the current is almost sine. The voltage of the inductor is measured. The result is shown in Fig. 13. The estimated value is acquired by multiplying the inductance [calculated from (11)] and sine current, which has the same RMS value of experimental current. The error is acceptable.

Combining (7) and (11), the inductance is designed with the variation range of 0.4–1.06 mH. The current ripple is calculated as shown in Fig. 5. The experimental result is also displayed in Fig. 14. The current ripple at the zero-crossing point is 2.9 A theoretically and 2.6 A practically. The current ripple at the peak value point is 4.5 A theoretically and 3.8 A practically, and the minimum current ripple is 1.7 A theoretically and 1.8 A

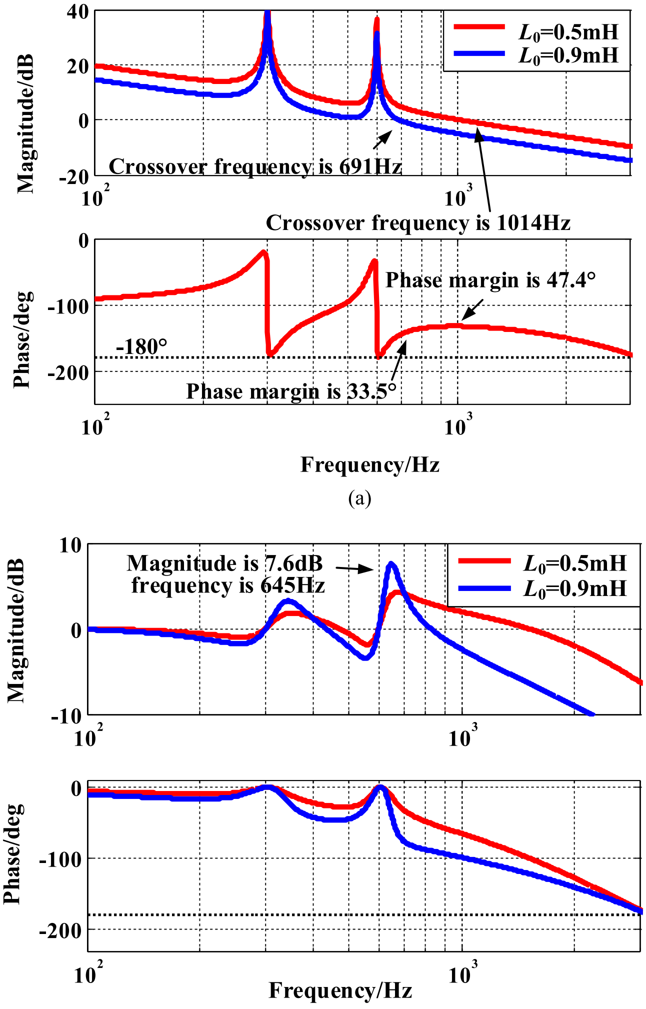

(a)

(b)

Fig. 15. Bode plot of the controller. (a) Open loop. (b) Closed loop.

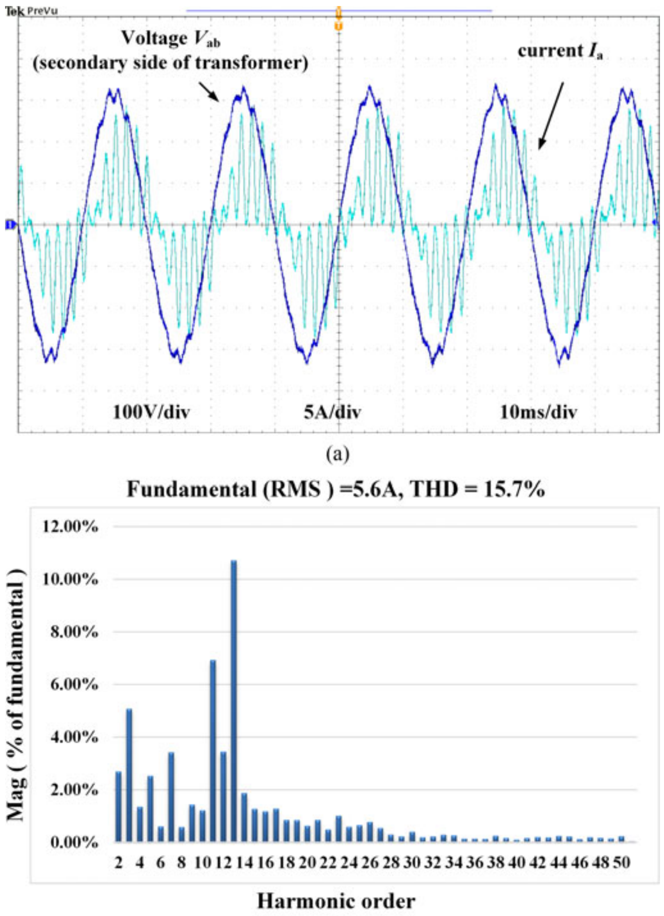

(a)

(b)

Fig. 16. Current waveform when the power is 1.67 kW. (a) Waveform. (b) THD analysis result.

practically. The estimated value is very close to the experimental result. The error may be caused by the following facts.

1) The inductance factor (A_L) has a tolerance. For example, magnetics powder cores are precision manufactured to an inductance factor tolerance of $\pm 8\%$ [9].
2) The measurement error is unavoidable especially the current spikes are obvious. For example, the minimum current ripple [shown in Fig. 14(b)] contains current spikes, making it hard to determine the accuracy value.
3) The experiment is performed under the condition of weak grid; the grid inductance also influences the current ripple.

The bode plots of the controller that has two resonance controllers and a PI controller are shown in Fig. 15. They are calculated according to the control block in Fig. 6. For full load, the effective inductance is 0.5 mH. The crossover frequency is 1014 Hz and the phase margin is 47.4°. This parameters can make the converter work well. For light load, the effective inductance is large (0.9 mH for 1.67 kW). Thus, the bandwidth becomes 691 Hz, and it is very close to the resonance frequency of the PR controller. There is a peak in the closed-loop bode plot when the load is light, as shown in Fig. 15(b). Thus, the converter performs badly in light load. The current waveform with the power of 1.67 kW is shown in Fig. 16. The current is distorted, and the 13th-order harmonic is the main component of the total harmonic distortion (THD) analysis result.

Fig. 17 shows the bode plot calculated from the transfer function. The PI parameters is tuned so that the converter can work well with light load. However, the crossover frequency is 2735 Hz when the converter works with the rated power, and the phase margin is not enough. The converter may fail with overload. The waveform of the current is shown in Fig. 18. The voltage is also distorted due to the leakage inductance of the transformer. The converter is unstable and the overcurrent protection works.

With the component $f(I_m)$ contained in the control loop, the bode plot is theoretically fixed, as shown in Fig. 19. It is calculated according to the control block shown in Fig. 9. The crossover frequency is 1100 Hz and the phase margin is 53°.

The waveform and THD analysis of the current only with the PI controller and with the proposed controller are shown in Figs. 20 and 21. Fifth-, seventh-, and 13 th-order harmonics are the main components for the PI controller as the THD analysis

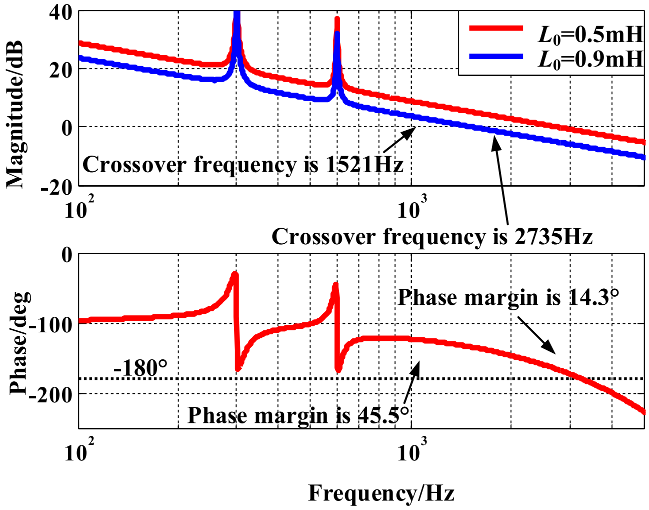

Fig. 17. Open-loop bode plot of the controller.

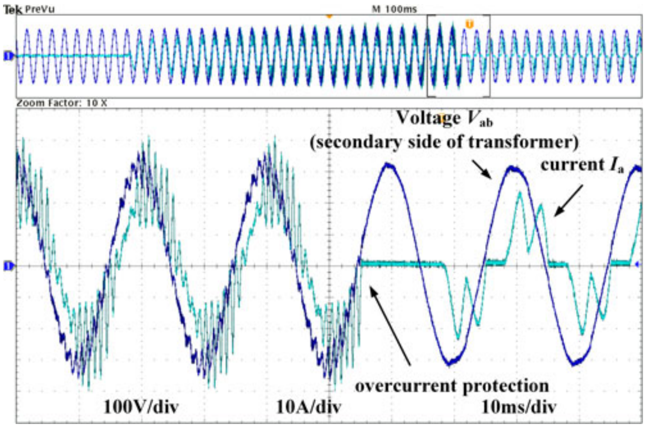

Fig. 18. Current waveform when the power is 6.6 kW and PI∗1.5.

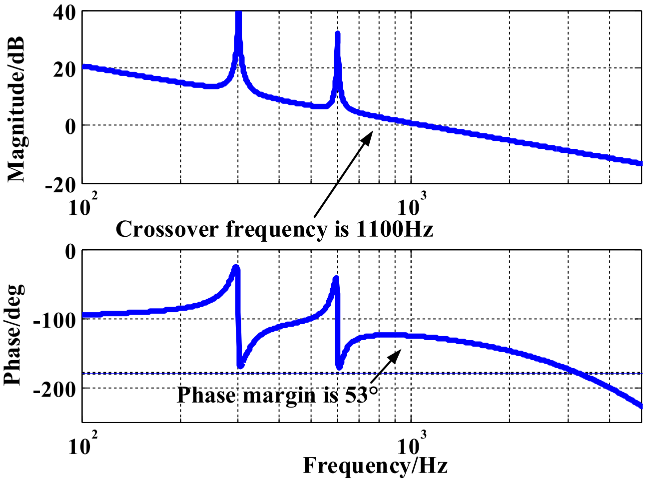

Fig. 19. Bode plot of the controller with $f\,(I_m)$.

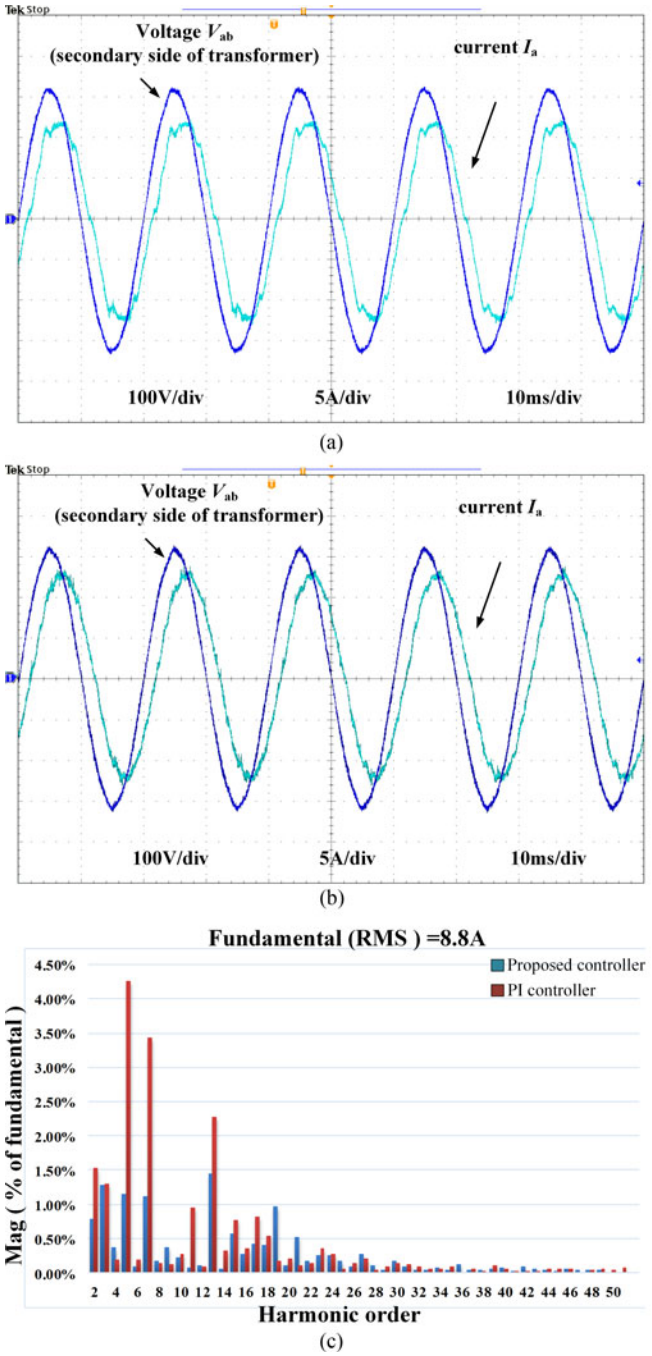

(a)

(b)

(c)

Fig. 20. Current waveform and THD analysis with half load. (a) Current waveform with the PI controller. (b) Current waveform with the proposed controller. (c) THD analysis results (THD = 6.5% for the PI controller and THD = 3.1% for the proposed controller).

shown in Figs. 20(c) and 21(c). Then, the fifth-, seventh-, and 13th-order harmonics are suppressed with the proposed controller from the experimental results. These results identify the analysis of the fluctuating inductor. It brings $(6k - 1)$-order negative-sequence and $(6k + 1)$-order positive-sequence harmonics. And the converter performs well under different output power. No instability tendency can be found in the results, which means the bandwidth does not change like before. The converter

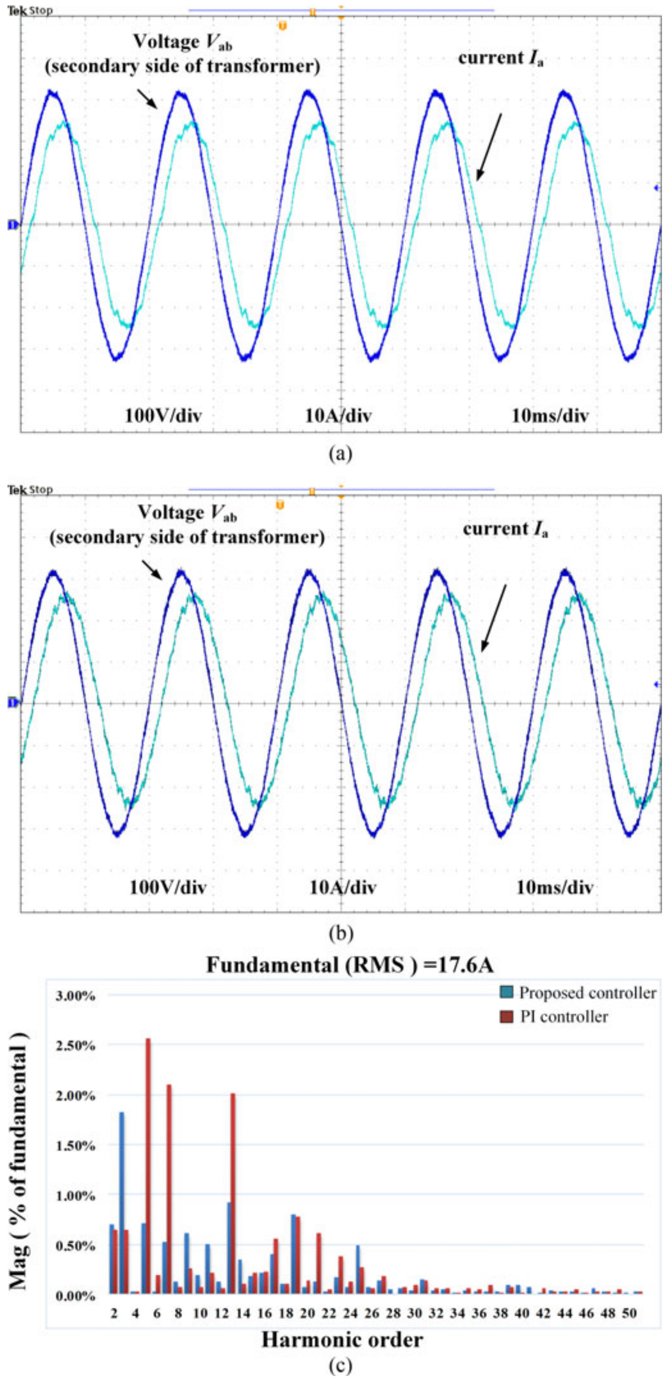

(a)

(b)

(c)

Fig. 21. Current waveform and THD analysis with full load. (a) Current waveform with the PI controller. (b) Current waveform with the proposed controller. (c) THD analysis results (THD = 4.2% for the PI controller and THD = 2.7% for the proposed controller).

can work well with the wide inductance variation of the powder core filter.

V. Conclusion

The powder core inductor is used for a three-phase inverter in this paper. Due to the soft-saturation nature of the powder core, the inductance will vary with current, making the performance of the inverter different. The current ripple and the controller for gird-connected converters considering the soft-saturation nature of the inductor are studied in this paper.

1) A smaller inductance can be obtained following the proposed inductance design principle, which is deduced from current ripple analysis. The maximum current ripple generally occurs at the point where the current reaches the peak value. The filter design principle considering the wide inductance variation is deduced. The inductances of three phases are different, as they correspond with the current. This violates the conventional design principle, making the design result of inductance larger than it should be. The inductance design result from the proposed inductance design principle is smaller.
2) The harmonic components for the three-phase converter with the powder core inductor are investigated. The model of the powder core inductor with the soft-saturation nature is developed, which is based on the Fourier series expansion. The inductance is divided into two parts: effective inductance and fluctuating inductances. It is proved that the fluctuating inductances will cause $(6k - 1)$-order negative-sequence and $(6k + 1)$-order positive-sequence harmonics, and the effective inductance determines the bandwidth of the controller.
3) A compensation method is proposed to eliminate the influence of inductance variation on the bandwidth. The mean value of the inductance (effective inductance) determines the bandwidth of the controller, and it corresponds to the amplitude of the current. So, for the light load, the bandwidth may be too close to the resonance frequencies of the PR controller, and for the full load, the bandwidth may be too large to have an enough phase margin. With the compensation method, the bandwidth can be fixed theoretically no matter how the load changes.

Experimental results verify the analysis and the feasibility of the proposed digital control.

References

[1] C. Liu, Y. Wang, J. Cui, Y. Zhi, M. Liu, and G. Cai, “Transformerless photovoltaic inverter based on interleaving high-frequency legs having bidirectional capability,” *IEEE Trans. Power Electron.*, vol. 31, no. 2, pp. 1131–1142, Feb. 2016.

[2] C. Zou, B. Liu, S. Duan, and R. Li, “Influence of delay on system stability and delay optimization of grid-connected inverters with LCL filter,” *IEEE Trans. Ind. Informat.*, vol. 10, no. 3, pp. 1775–1784, Aug. 2014.

[3] M. J. Duran, I. Gonzalez Prieto, M. Bermudez, F. Barrero, H. Guzman, and M. R. Arahal, “Optimal fault-tolerant control of six-phase induction motor drives with parallel converters,” *IEEE Trans. Ind. Electron.*, vol. 63, no. 1, pp. 629–640, Jan. 2016.

[4] K. Ma, W. Chen, M. Liserre, and F. Blaabjerg, “Power controllability of a three-phase converter with an unbalanced AC source,” *IEEE Trans. Power Electron.*, vol. 30, no. 3, pp. 1591–1604, Mar. 2015.

[5] J. Liu, S. Vazquez, L. Wu, A. Marquez, H. Gao, and L. G. Franquelo, “Extended state observer-based sliding-mode control for three-phase power converters,” *IEEE Trans. Ind. Electron.*, vol. 64, no. 1, pp. 22–31, Jan. 2017.

[6] S. Debnath, J. Qin, B. Bahrani, M. Saeedifard, and P. Barbosa, “Operation, control, and applications of the modular multilevel converter: A review,” *IEEE Trans. Power Electron.*, vol. 30, no. 1, pp. 37–53, Jan. 2015.

[7] X. Wang, F. Blaabjerg, and W. Wu, “Modeling and analysis of harmonic stability in an AC power-electronics-based power system,” *IEEE Trans. Power Electron.*, vol. 29, no. 12, pp. 6421–6432, Dec. 2014.

[8] T.-F. Wu, H.-S. Nien, C.-L. Shen, and T.-M. Chen, “A single-phase inverter system for PV power injection and active power filtering with nonlinear inductor consideration,” *IEEE Trans. Ind. Appl.*, vol. 41, no. 4, pp. 1075–1083, Jul./Aug. 2005.

[9] *Magnetics Powder Core Catalog*, *Magnetics Int.*, Burns Harbor, IN, USA, 2015.

[10] M. Gu, S. Ogasawara, and M. Takemoto, “Novel PWM Schemes with multi SVPWM of sensorless IPMSM drives for reducing current ripple,” *IEEE Trans. Power Electron.*, vol. 31, no. 9, pp. 6461–6475, Sep. 2016.

[11] D. Jiang and F. Wang, “Current-ripple prediction for three-phase PWM converters,” *IEEE Trans. Ind. Appl.*, vol. 50, no. 1, pp. 531–538, Jan./Feb. 2014.

[12] Y. Jiao and F. C. Lee, “LCL filter design and inductor current ripple analysis for a three-level NPC grid interface converter,” *IEEE Trans. Power Electron.*, vol. 30, no. 9, pp. 4659–4668, Sep. 2015.

[13] A. Hilal, M. A. Raulet, C. Martin, and F. Sixdenier, “Power loss prediction and precise modeling of magnetic powder components in DC–DC power converter application,” *IEEE Trans. Power Electron.*, vol. 30, no. 4, pp. 2232–2238, Apr. 2015.

[14] S. Jayalath, D. Ongayo, and M. Hanif, “Modelling powder core inductors for passive filters in inverters using finite element analysis,” *Electron. Lett.*, vol. 53, no. 3, pp. 179–181, Feb. 2, 2017.

[15] S. C. Chung, S. R. Huang, J. S. Huang, and E. C. Lee, “Applications of describing functions to estimate the performance of nonlinear inductance,” *IEE Proc.—Sci., Meas. Technol.*, vol. 148, no. 3, pp. 108–114, May 2001.

[16] R. A. Mastromauro, M. Liserre, and A. Dell’Aquila, “Study of the effects of inductor nonlinear behavior on the performance of current controllers for single-phase PV grid converters,” *IEEE Trans. Ind. Electron.*, vol. 55, no. 5, pp. 2043–2052, May 2008.

[17] H. Safamehr, T. A. Najafabadi, and F. R. Salmasi, “Enhanced control of grid-connected inverters with non-linear inductor in LCL filter,” *IET Power Electron.*, vol. 9, no. 10, pp. 2111–2120, Aug. 17, 2016.

[18] T. F. Wu, K. H. Sun, C. L. Kuo, and C. H. Chang, “Predictive current controlled 5-kW single-phase bidirectional inverter with wide inductance variation for DC-microgrid applications,” *IEEE Trans. Power Electron.*, vol. 25, no. 12, pp. 3076–3084, Dec. 2010.

[19] T. F. Wu, P. H. Lee, L. C. Lin, C. H. Chang, and Y. K. Chen, “Circulating current reduction for three-phase back-to-back transformerless inverter with SPWM-based D-Σ digital control,” *IEEE Trans. Power Electron.*, vol. 32, no. 2, pp. 1591–1601, Feb. 2017.

[20] T. F. Wu, C. H. Chang, L. C. Lin, Y. C. Chang, and Y. R. Chang, “Two-phase modulated digital control for three-phase bidirectional inverter with wide inductance variation,” *IEEE Trans. Power Electron.*, vol. 28, no. 4, pp. 1598–1607, Apr. 2013.

[21] T. F. Wu, C. H. Chang, L. C. Lin, G. R. Yu, and Y. R. Chang, “A D-Σ digital control for three-phase inverter to achieve active and reactive power injection,” *IEEE Trans. Ind. Electron.*, vol. 61, no. 8, pp. 3879–3890, Aug. 2014.

[22] T. F. Wu, H. C. Hsieh, C. H. Chang, L. C. Lin, and Y. R. Chang, “Improvement of control law derivation and region selection for D-Σ digital control,” *IEEE Trans. Ind. Electron.*, vol. 62, no. 10, pp. 6042–6050, Oct. 2015.

[23] T. F. Wu, L. C. Lin, N. Yao, Y. K. Chen, and Y. C. Chang, “Extended application of D-Σ digital control to a single-phase bidirectional inverter with an LCL filter,” *IEEE Trans. Power Electron.*, vol. 30, no. 7, pp. 3903–3911, Jul. 2015.

[24] T. F. Wu, H. C. Hsieh, C. W. Hsu, and Y. R. Chang, “Three-phase three-wire active power filter with D-Σ digital control to accommodate filter-inductance variation,” *IEEE J. Emerg. Sel. Topics Power Electron.*, vol. 4, no. 1, pp. 44–53, Mar. 2016.

[25] M. Liserre, Teodorescu, and F. Blaabjerg, “Stability of photovoltaic and wind turbine grid-connected inverters for a large set of grid impedance values,” *IEEE Trans. Power Electron.*, vol. 21, no. 1, pp. 263–272, Jan. 2006.

[26] X. Wang, P. C. Loh, and F. Blaabjerg, “Stability analysis and controller synthesis for single-loop voltage-controlled VSIs,” *IEEE Trans. Power Electron.*, vol. 32, no. 9, pp. 7394–7404, Sep. 2017.

[27] D. Pérez-Estévez, J. Doval-Gandoy, A. G. Yepes, and Ó. López, “Positive- and negative-sequence current controller with direct discrete-time pole placement for grid-tied converters with LCL filter,” *IEEE Trans. Power Electron.*, vol. 32, no. 9, pp. 7207–7221, Sep. 2017.

[28] X. Zhang, Z. Fu, Y. Xiao, G. Wang, and D. Xu, “Control of parallel three-phase PWM converters under generalized unbalanced operating conditions,” *IEEE Trans. Power Electron.*, vol. 32, no. 4, pp. 3206–3215, Apr. 2017.

Qikang Wei received the B.S. degree in electrical engineering in 2013 from the Huazhong University of Science and Technology, Wuhan, China, where he is currently working toward the Ph.D. degree with the school of Electrical and Electronics Engineering.

His research interests include renewable energy applications and large-capacity inverters.

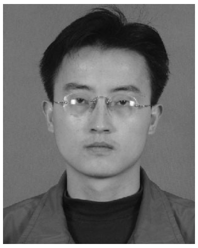

Bangyin Liu (M’10) received the B.S., M.S., and Ph.D. degrees in electrical engineering from the Huazhong University of Science and Technology (HUST), Wuhan, China, in 2001, 2004, and 2008, respectively.

From 2008 to 2010, he was a Postdoctoral Research Fellow with the Department of Control Science and Engineering, HUST, where he is currently an Associate Professor with the School of Electrical and Electronics Engineering. His current research interests include renewable energy applications, power quality, and power electronics applied to power systems.

Shanxu Duan (M’14–SM’16) received the B.S., M.S., and Ph.D. degrees in electrical engineering from the Huazhong University of Science and Technology, Wuhan, China, in 1991, 1994, and 1999, respectively.

Since 1991, he has been a faculty member with the College of Electrical and Electronics Engineering, Huazhong University of Science and Technology, where he is currently a Professor. His research interests include stabilization, nonlinear control with application to power electronic circuits and systems, fully digitalized control techniques for power electronics apparatus and systems, and optimal control theory and corresponding application techniques for high-frequency pulse-width-modulation power converters.

Dr. Duan is a senior member of the Chinese Society of Electrical Engineering and a council member of the Chinese Power Electronics Society. He was selected as one of the New Century Excellent Talents by the Ministry of Education of China in 2007. He was also the recipient of the honor of “Delta Scholar” in 2009.